RSC Advances

ROYAL SOCIETY OF CHEMISTRY

PAPER

View Article Online
View Journal | View Issue

Cite this: *RSC Adv.*, 2026, **16**, 12841

Sustainable photocatalytic removal of cosmetic preservative parabens over a dual S-scheme TiO_2/ZnO/g-C_3N_4 catalyst under natural sunlight irradiation

Mano Ranjan Barik, Anshuman Sarangi and Sushanta Kumar Badamali *

Received 28th January 2026
Accepted 3rd March 2026

DOI: 10.1039/d6ra00767h

rsc.li/rsc-advances

Parabens, such as MeP or EtP, are common ingredients of widely used synthetic preservatives in cosmetics or personal care products. Extensive use of those products eventually leads to their persistence in aquatic environments, posing ecological and health risks. In the present work, a ternary dual S-scheme photocatalyst, TiO_2/ZnO/g-C_3N_4 (TZC), was rationally synthesized and comprehensively characterized using XRD, FTIR, FESEM, HRTEM, XPS, TGA, UV-vis DRS, PL, and N_2 sorption analyses. The results confirmed the successful construction of a well-coupled heterojunction with optimized band alignment, facilitating efficient charge transfer and visible-light utilization. Under sunlight irradiation, the TZC composite exhibited markedly enhanced photocatalytic activity, achieving 97.6% and 98.3% degradation of MeP and EtP, respectively, within 90 min of sunlight exposure. Kinetic analysis revealed first-order degradation behaviour, while radical quenching experiments identified $^{\bullet}OH$ as the predominant reactive oxygen species responsible for the photocatalytic oxidation of parabens. The superior performance was attributed to the synergistic effects of the dual S-scheme charge transfer, which promoted the spatial separation of photogenerated charge carriers and preserved a strong redox potential. The heterogeneity test showed the catalyst was purely active in the solid phase and recyclable up to six cycles with a marginal decrease in efficiency of ~8%. Furthermore, LC-MS analysis enabled the identification of intermediate degraded species, and a plausible degradation pathway was proposed. This study not only demonstrates the efficacy of a dual S-scheme TZC heterojunction in the solar-driven removal of cosmetic parabens but also provides mechanistic insights into its potential for sustainable water purification applications.

1. Introduction

The demand for carbon-based compounds is continuously increasing because of their effectiveness, stability, and wide range of functionality. They play a vital role in multiple sectors, such as agriculture, pharmaceuticals, food preservation, cosmetic industries, *etc.*[1,2] Cosmetic products are essential commodities widely used for enhancing personal cleanliness, improving appearance, and boosting self-confidence. To meet the diverse needs of consumers worldwide, a variety of products are available, ranging from skincare and haircare formulations to makeup and perfumes.[3] The extensive use of personal care products and cosmetics has raised substantial environmental concerns due to their stability and persistence in aquatic ecosystems.[4,5]

In the cosmetic industry, parabens are widely used as preservatives to prevent microbial growth, increase shelf life, and ensure consumer safety. Their antimicrobial properties make them effective against bacteria, yeast, and molds, which can otherwise cause product spoilage and pose health risks.[6] Due to their stability, cost-effectiveness, and compatibility with various cosmetic formulations, parabens have become a key component in the global cosmetics industry. The global cosmetics industry has witnessed significant expansion over the years, with an estimated market value exceeding \$500 billion. In India, the cosmetics market is projected to reach \$18.4 billion by 2032, growing at a CAGR of 3.2% from 2024 to 2032.[7] The increasing consumer inclination towards personal care and beauty products, coupled with the influence of social media and celebrity endorsements, has fuelled this growth.

Despite concerns regarding the potential health and environmental risks of parabens, their use persists due to the lack of equally effective and affordable alternatives. Regulatory agencies such as the U.S. Food and Drug Administration (FDA) and the European Medicines Agency (EMA) continue to evaluate the safety of parabens in cosmetics, leading to evolving regulations and the emergence of paraben-free product lines.[8,9]

Department of Chemistry, Utkal University, Vani Vihar, Bhubaneswar, 751004, Odisha, India. E-mail: skbuche@utkaluniversity.ac.in

Among the parabens, the presence of methylparaben (MeP) and ethylparaben (EtP) in many cosmetic products has raised concerns due to their very long term stability and potential existence in the environment after use. These chemicals can mimic estrogen in the body, leading to disrupted hormone function, and are classified as endocrine-disrupting compounds (EDC) in living organisms.[10–12] Research has shown that continuous exposure to MeP and EtP can lead to hormonal imbalances, breast cancer, reproductive/developmental abnormalities, and their potential bioaccumulation raises further concerns about long-term ecological impacts.[13,14]

Various remediation methods have been explored to eliminate parabens from contaminated water streams. These methods include adsorption, electrochemical, phytoremediation, and advanced oxidation processes.[15,16] Photocatalytic degradation stands out due to its efficiency, selectivity, and sustainability. It harnesses light energy to degrade parabens, offering a low-cost and eco-friendly solution.[17,18] The basic principle of photocatalysis involves light absorption and the excitation of electrons from the valence band to the conduction band, leaving behind holes in the valence band of the semiconducting material. These electrons and hole pairs react with oxygen and water, forming reactive species like hydroxyl radicals and superoxide ions.[19–23] These species degrade pollutants into either less harmful byproducts, eventually into carbon dioxide and water. Conventional photodegradation methods face several challenges, including limited light absorption, rapid recombination of charge carriers, and low quantum yield. Among them, recombination is a major obstacle in photocatalysis, occurring when photogenerated charge carriers (electrons and holes) recombine instead of participating in redox reactions. This reduces photocatalytic efficiency, as the energy is dissipated as heat or light, rather than driving chemical reactions to degrade pollutants.[24,25]

To overcome these challenges, the use of heterojunction photocatalysts has emerged as a superior approach compared to conventional methods. Heterojunctions are prepared by combining two or more semiconductors, which can efficiently separate photogenerated charge carriers, reducing recombination and enhancing photocatalytic activity.[26,27] This leads to improved light absorption, increased quantum efficiency, and better stability. Heterojunction photocatalysts have shown remarkable performance in degrading pollutants, making them a promising solution for environmental remediation. Their versatility and tunability also offer opportunities for tailored design and optimization of their potential.

Photocatalysts such as TiO_2, ZnO, and g-C_3N_4 have individually shown promise for the degradation of parabens under UV or visible light. Titanium dioxide (TiO_2) is a widely used photocatalyst due to its strong oxidative power, chemical stability, and non-toxicity.[28] Similarly, the wide bandgap energy, high electron mobility, and high stability of ZnO enable efficient photocatalytic reactions, making it a rational choice for water treatment and environmental remediation.[29] On the other hand, g-C_3N_4 is a promising visible-light photocatalyst with potential applications in photocatalysis.[30] However, in the case of individual photocatalysts, possible recombination of charge carriers reduces their catalytic efficiency. To reduce the recombination and enhance activity, the formation of heterojunction photocatalysts comes as a standout option. The dual S-scheme TZC heterojunction is a promising material, leveraging the strengths of each material, such as the UV absorption of ZnO, the redox ability of TiO_2, and the visible light absorption capacity of g-C_3N_4, making it the best solar light photocatalyst.[31,32] This synergy suppresses recombination, amplifying photocatalytic efficiency and rendering it a potential solution for environmental remediation.

Researchers have investigated the photocatalytic degradation of ethyl paraben (EtP) under diverse operational conditions, revealing both promising outcomes and notable challenges that limit real-world applicability. Petala *et al.* demonstrated that Cu incorporation into $BiVO_4$ significantly enhanced photocatalytic activity, achieving an impressive 98% degradation of 1.5 mg L^{-1} EtP within 1 h; however, efficiency dropped to 79% when the pollutant concentration increased to 7.5 mg L^{-1}, suggesting that active-site saturation and light-attenuation effects hinder performance at higher loads.[33] Frontistis *et al.* reported 90% degradation of EtP using Ag_3PO_4 under simulated solar light in 60 min, yet the photocatalyst's pronounced photo instability and susceptibility to photo corrosion severely compromise its recyclability and long-term operational stability.[34] Liu *et al.* synthesized a $Bi_2Ti_2O_7/TiO_2$ composite *via* a molecularly imprinted sol–gel approach and achieved 81.4% removal of 10 mg L^{-1} EtP, though the overall efficiency and scalability of molecular imprinting remain limited for practical wastewater treatment applications.[35] Collectively, these studies highlight persistent limitations in existing systems, including concentration-dependent efficiency losses, catalyst instability under illumination, photo corrosion, and insufficient degradation at higher pollutant levels. Thus, the development of a highly stable, efficient, and sustainable photocatalyst capable of delivering consistent performance across a wide range of reaction conditions remains an urgent research need for effective EtP remediation.

The objective of this study is to investigate the synergistic photocatalytic performance of a newly designed TiO_2/ZnO/g-C_3N_4 (TZC) ternary heterostructure for the efficient degradation of ethyl paraben, a persistent endocrine-disrupting compound of emerging environmental concern. Although TiO_2, ZnO, and g-C_3N_4 are well-established photocatalysts, their controlled integration into a dual S-scheme heterojunction is expected to markedly enhance photocatalytic functionality by strengthening visible-light absorption, promoting directional charge migration, and maximizing the formation of high-energy electrons and strongly oxidizing holes. The dual S-scheme configuration not only suppresses rapid charge recombination but also preserves the redox potentials of the terminal photocatalysts, enabling the simultaneous generation of reactive oxygen species such as $^{\bullet}O_2^-$ and $^{\bullet}OH$ those are critical for degrading stable aromatic pollutants like parabens. Additionally, the S-scheme-based photocatalytic system improves interfacial charge transfer pathways, enhances stability against photo corrosion, and supports sustained catalytic activity during long-term irradiation. This developed catalyst to be employed for the photocatalytic degradation of underexplored parabens in an aqueous environment. Overall, the present work is an attempt to offer a cost-effective and environmentally benign route for fabricating a robust, visible-light-responsive photocatalyst, further emphasizing its strong potential for practical and scalable wastewater remediation applications.

2. Experimental

2.1 Reagent and catalyst

Ethyl paraben and methyl paraben (BLD Pharmatech, 99.19%), urea (SRL, 99.5%), hydrochloric acid (Merck Life Science, 35%), zinc nitrate hexahydrate (SRL, 98%), ethanol (AR, China, 99.9%), and titanium isopropoxide (Sigma-Aldrich, 97%) were used as received. Deionized water was employed as the reaction medium throughout the study.

2.2 Preparation of g-C_3N_4 sheet from urea

The synthesis of graphitic carbon nitride (g-C_3N_4) was carried out by direct thermal polycondensation of urea as reported earlier.[36] In a typical procedure, 15 g of urea was placed in a 50 mL crucible and calcined in a muffle furnace. The crucible was covered with lid followed by wrapping by aluminium foil and heated to final temperatures of 550 °C for 3 h at a ramp rate of 5 °C min^{-1}. After cooling, the resulting yellowish powder was thoroughly washed with 1 M hydrochloric acid and deionized water to ensure complete removal of the residual alkaline species. The washed material was then filtered and dried at 80 ° C for 12 h. To ensure purity, the dried product was further heated at 400 °C for 3 h to eliminate salts impurities that may have formed during acid treatment.

2.3 Preparation of ZnO/TiO_2/g-C_3N_4 (TZC) xerogel

The synthesis of the TZC was presented in Scheme 1. In a typical preparation process, solutions of titanium and g-C_3N_4 precursors were prepared and combined as per the details provided below. Solution A consisted of 5 mL of titanium isopropoxide mixed with 15 mL of ethanol. Solution B contained 10 mL of distilled water, 10 mL of ethanol, and 200 mg of g-C_3N_4, and was stirred for 80 min. Subsequently, an appropriate molar amount of Zinc nitrate was added (corresponding to 10% ZnO) to solution B and stirred for another 30 min. After this, solution A was gradually added to solution B under continuous stirring for 5 h at room temperature. The mixture was then allowed to stand undisturbed for 24 h, resulting in the formation of a TiO_2 xerogel. The xerogel was calcined at 400 °C for 3 h to achieve densification, remove volatile species, and obtain the final TZC heterostructure. In a similar process, TiO_2/g-C_3N_4 (TC) was prepared without adding the precursor of zinc.

2.4 Characterization

The catalyst was characterized symmetrically to understand the structural, elemental, electronic, optical, and morphological properties. Structural properties of TZC were studied by an X-ray diffractometer (PANanalytical diffractometer) using monochromatic Cu Kα ($\lambda = 1.54$ Å) radiation. Fourier Transform Infrared Spectroscopy is used to detect functional groups and bonding interactions, generally recorded in the range of 400–4000 cm^{-1} to observe vibrations of metal–oxygen bonds and g-C_3N_4 structure. Surface morphology and particle distribution were studied by Field Emission Scanning Electron Microscope (Ziess machine 5kV). High-Resolution Transmission Electron Microscope (PHI LIPS CM 200) was used to observe the crystal structure and lattice fringes at the nanoscale, operating at an accelerating voltage of 200 kV. X-ray photoelectron spectra measurements were obtained using an Omicron ESCA system (Oxford Instruments, Germany). For the analysis of surface area, pore volume, and pore size distribution of the TZC sample, the sample was outgassed at 180 °C for 8 h, and a Quantachrome instrument was used for the evaluation. UV-vis spectroscopy (PerkinElmer, Germany) is employed to evaluate optical properties and bandgap energies in the wavelength range of 200–800 nm. Photoluminescence (PL) (Edinburgh FLS 980S photoluminescence spectrophotometer) spectroscopy is carried out typically at room temperature with an excitation wavelength around 330 nm to assess the recombination rate of photoexcited electron–hole pairs. For the analysis of fragments obtained during the photocatalytic reaction Agilent 6530 Q-TOF LC MS system was employed.

2.5 Catalytic activity studies

Photocatalytic experiments were performed in the early summer (February to May) under direct natural sunlight on clear, cloud-free days between 10:00 AM and 2:00 PM to ensure stable and high solar irradiance. The experiments were conducted at the location (Bhubaneswar, India; latitude: 20.300622°, longitude: 85.842409°), which receives an average solar irradiance of 4.8–5.0 kWh m^{-2} per day, corresponding to an instantaneous light intensity of approximately 95–100 mW cm^{-2}. For optimized degradation reaction, 50 mL of EtP solution (10 mg L^{-1}) was mixed with 50 mg of photocatalyst and magnetically stirred in the dark for 20 min to establish adsorption–desorption equilibrium. After equilibration, the suspension was exposed to sunlight for 90 min to initiate the photocatalytic reaction. Aliquots of 5 mL were collected every 30 min, followed by centrifugation for 15 min to separate the solid catalyst. The extent of degradation was quantified by monitoring the fall in absorbance at $\lambda_{\max} = 255$ nm using a UV-vis spectrophotometer (Agilent Cary 200, USA). Catalyst loading and initial EtP concentration were systematically varied to determine the optimal photocatalytic conditions.

The extent of EtP degradation was quantified by using the formulae

$$\text{Degradation}(\%) = \frac{C_0 - C_t}{C_0} \times 100 \tag{1}$$

where C_0 and C_t are the concentrations of the reaction mixture at the commencement and after a definite interval of time t, respectively, and the concentrations are proportional to the absorbance values.

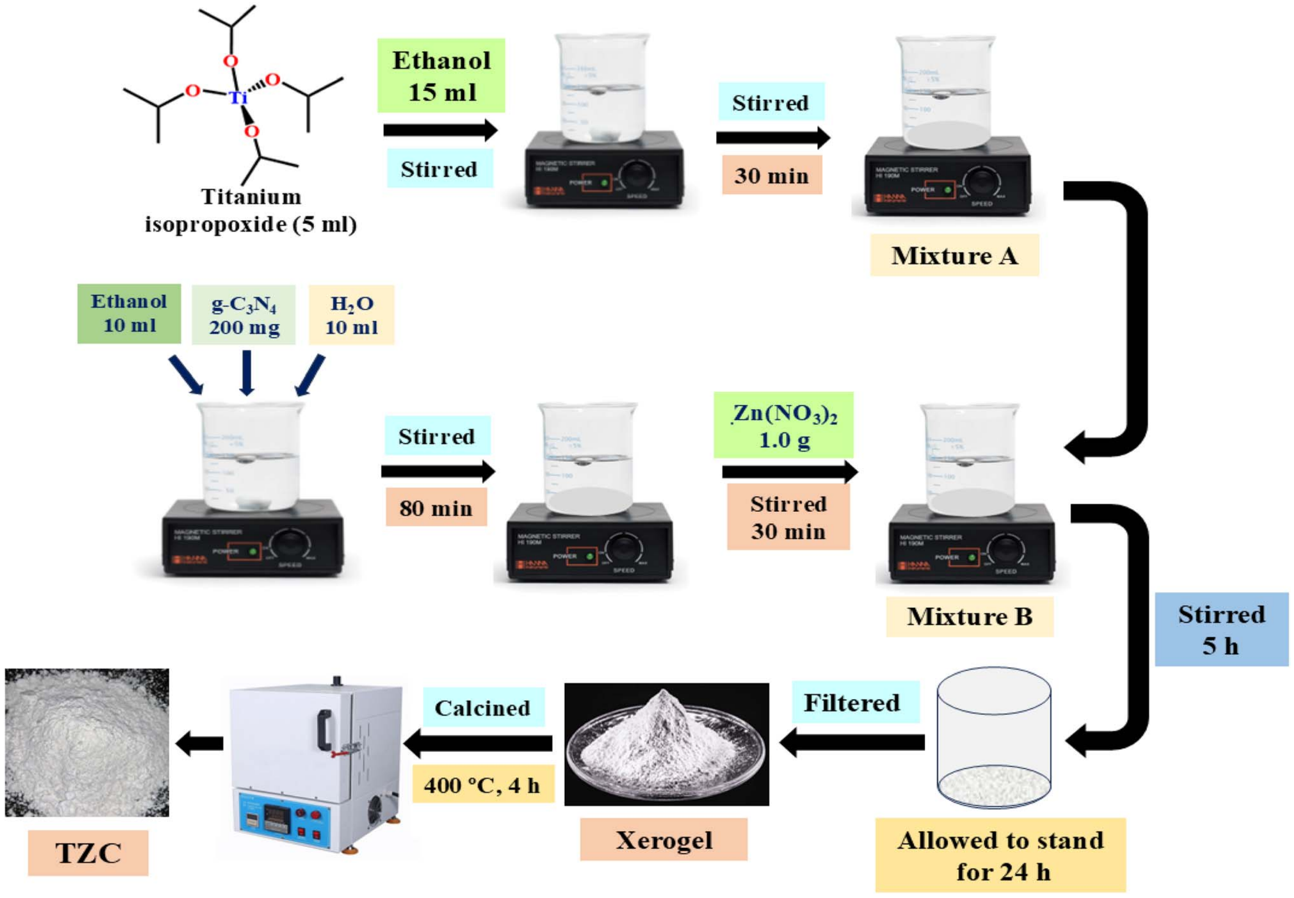

Scheme 1 Preparation of the TZC heterojunction.

To evaluate the heterogeneity of the catalyst, the photocatalytic degradation study was conducted using the filtrate of the catalysts. The catalyst was stirred in water for 90 min to obtain a filtrate after separating from the solid residue. Both components, the filtrate and the isolated solid catalyst, were independently assessed for EtP degradation under identical reaction conditions. Reusability studies were conducted to ascertain the catalyst stability. After each photocatalytic run, the catalyst was recovered by centrifugation, washed thoroughly with deionized water to remove surface-adsorbed residues, dried, and subsequently regenerated. The regenerated material was used in successive cycles to examine its durability and photocatalytic performance over multiple runs.

3. Results and discussion

3.1 Catalyst characterization

3.1.1 XRD analysis. The X-ray diffraction (XRD) analysis was employed to elucidate the crystalline phases and structural features of the developed materials. The detailed XRD patterns are presented in Fig. 1a. The diffraction pattern of TiO_2 displays well-defined reflections characteristic of the anatase phase, with prominent peaks at 25.4, 37.8, and 48.1°, corresponding to the (101), (004), and (200) planes, respectively, confirming its high degree of crystallinity.[37] ZnO exhibits sharp and intense peaks indexed to the wurtzite structure, including the (100), (002), (102), and (311) planes at 32.1, 34.6, 36.5, and 56.7°, respectively.[38] The g-C_3N_4 sample shows its typical (002) diffraction peak at 27.4°, associated with interlayer stacking in its graphitic framework. The TC heterostructure clearly displays the characteristic peaks of both TiO_2 and g-C_3N_4, indicating successful integration of the two components. In the TZC heterostructure, reflections corresponding to TiO_2, ZnO, and g-C_3N_4 are simultaneously observed, confirming the formation of the ternary composite. Notably, slight peak broadening and minor shifts in diffraction positions are evident, which can be attributed to strong interfacial coupling among the three phases.

3.1.2 FT IR analysis. The FTIR analysis provides essential insight into the functional groups and interfacial interactions present in the synthesized photocatalyst. The FTIR spectrum of the TZC composite displays the characteristic vibrational features of its constituent materials, confirming successful ternary integration (Fig. 1b). In the 400–700 cm^{-1} region, distinct Ti–O and Zn–O stretching bands verify the incorporation of TiO_2 and ZnO.[39] The absorption region between 1200 and 1650 cm^{-1} exhibits multiple C–N and C=N stretching signals associated with the heptazine units of g-C_3N_4, while a weak band near 2340 cm^{-1} corresponds to atmospheric CO_2.[40] Broad absorptions in the 3000–3600 cm^{-1} range arise from O–H and/or N–H stretching vibrations, indicating surface-adsorbed

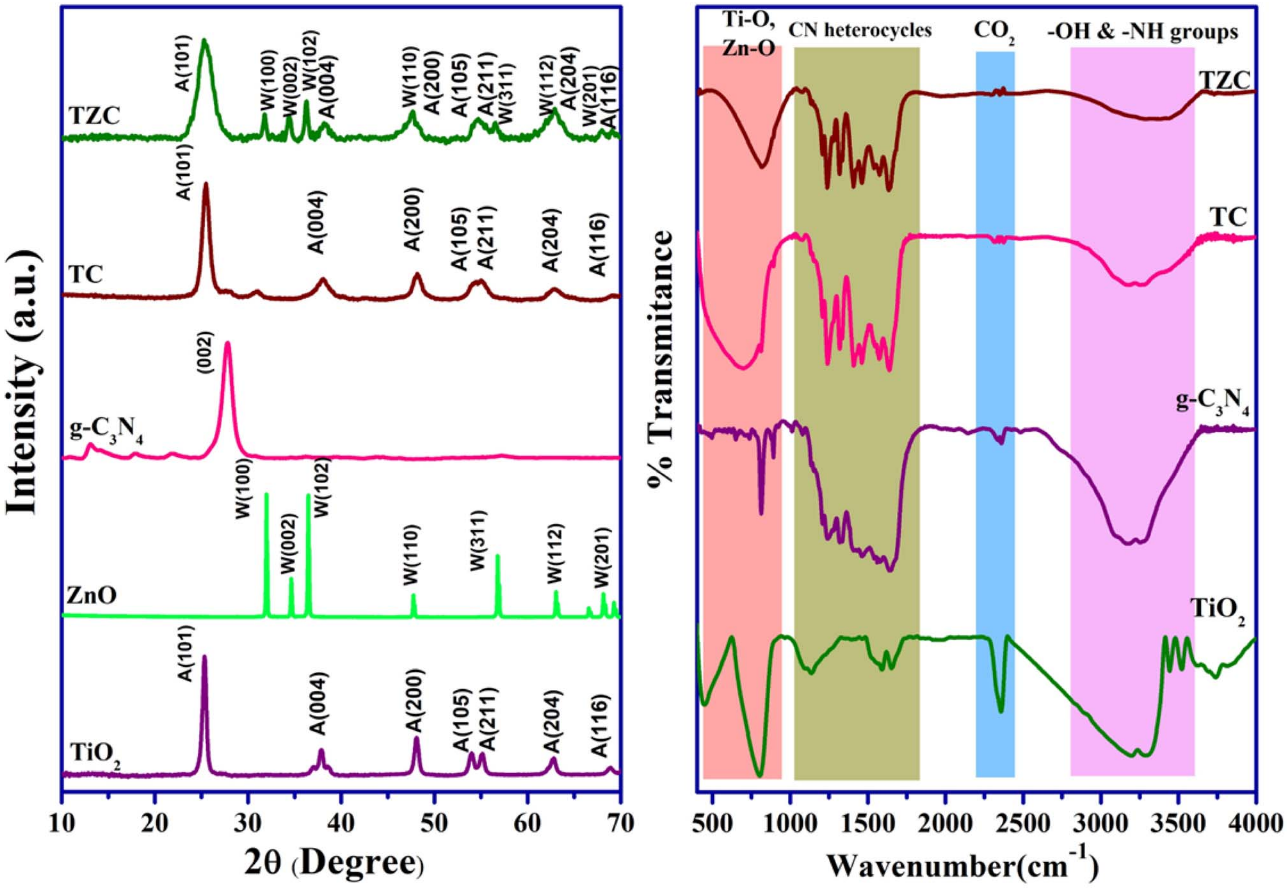

Fig. 1 XRD (a) and FT IR (b) analysis of photocatalysts.

moisture and terminal amine groups. These spectral features collectively confirm the successful formation of the TZC ternary system, with enhanced interfacial interactions that are expected to contribute to its improved photocatalytic performance.

3.1.3 FE SEM analysis. The surface morphology of the synthesized materials was examined using FE SEM, and the corresponding images are presented in Fig. 2. Pure TiO_2 (Fig. 2a) exhibits uniformly distributed, spherical nanoparticles with an average particle size of ~85 nm and a high packing density. In contrast, g-C_3N_4 (Fig. 2b) displays a layered, sheet-like morphology arising from its graphitic framework, providing extended surface exposure and facilitating interfacial charge migration. The ternary TZC composite (Fig. 2c) reveals a well-integrated architecture in which TiO_2 nanoparticles and ZnO grains are anchored onto the g-C_3N_4 sheets, establishing intimate heterojunction interfaces among the three components. This interconnected structure is indicative of strong interfacial coupling, which is expected to enhance charge separation efficiency and support the dual S-scheme mechanism. The EDAX spectrum and elemental mapping (Fig. S1, SI) confirm the presence and uniform distribution of Ti, Zn, O, C, and N throughout the composite, validating the successful formation of the TZC heterostructure. The consistent dispersion of metal oxides within the g-C_3N_4 matrix underscores the structural integrity of the composite.

3.1.4 HR TEM analysis. The HR TEM pattern shown in Fig. 3 provides vital insight into the nanoscale architecture and crystallographic features of the TZC heterojunction. HR TEM analysis (Fig. 3a and b) reveals that the heterostructure consists of nanoparticles anchored onto a thin, sheet-like matrix, confirming the successful integration of TiO_2, ZnO, and g-C_3N_4 within a unified heterostructure. Higher-magnification images in Fig. 3c clearly show lattice fringes with distinct interplanar spacings corresponding to the different phases present in the composite. Estimated *d*-spacings of 0.35, 0.28, 0.24, and 0.32 nm can be indexed to the (101) reflection of anatase TiO_2, the (100) and (102) reflections of wurtzite ZnO, and the (002) reflection of g-C_3N_4, respectively, thereby confirming the polycrystalline nature of the material. The intimate contact between these lattice fringes strongly indicates the formation of effective heterointerfaces, which are essential for facilitating directional charge transfer in the dual S-scheme system. The selected-area electron diffraction (SAED) pattern in Fig. 3d exhibits concentric diffraction rings corresponding to the (101), (004), (200), (102), and (002) reflections of the constituent materials, further validating the polycrystalline nature of the TZC composite. The coexistence of well-resolved lattice fringes and distinct SAED rings demonstrated the structural integrity and strong interfacial coupling within the heterojunction.

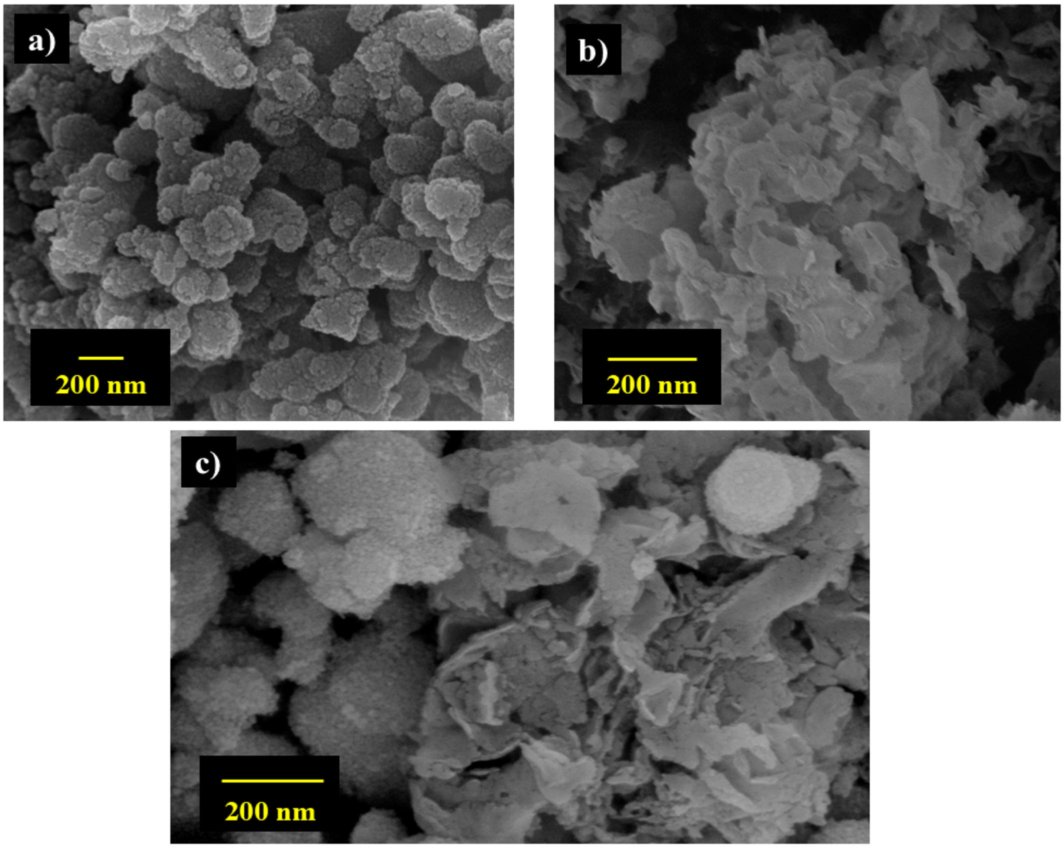

Fig. 2 FE SEM images of TiO_2 (a), g-C_3N_4 (b), and TZC (c).

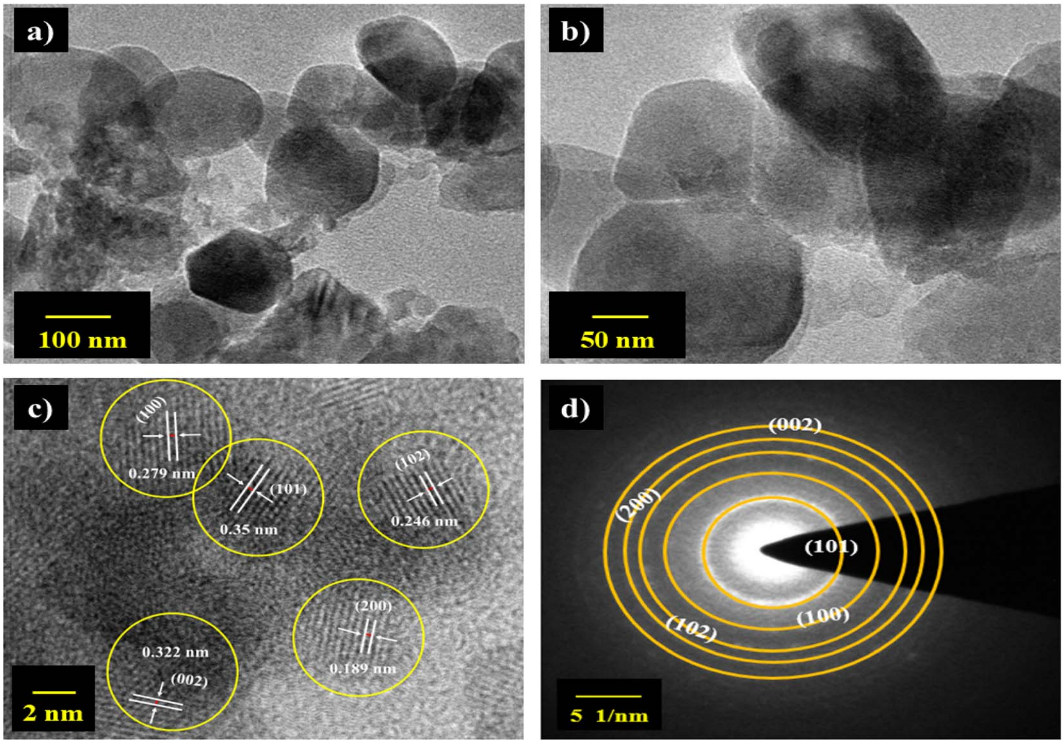

Fig. 3 HR TEM images (a and b), lattice fringe at higher magnification (c), and SAED pattern (d) of TZC.

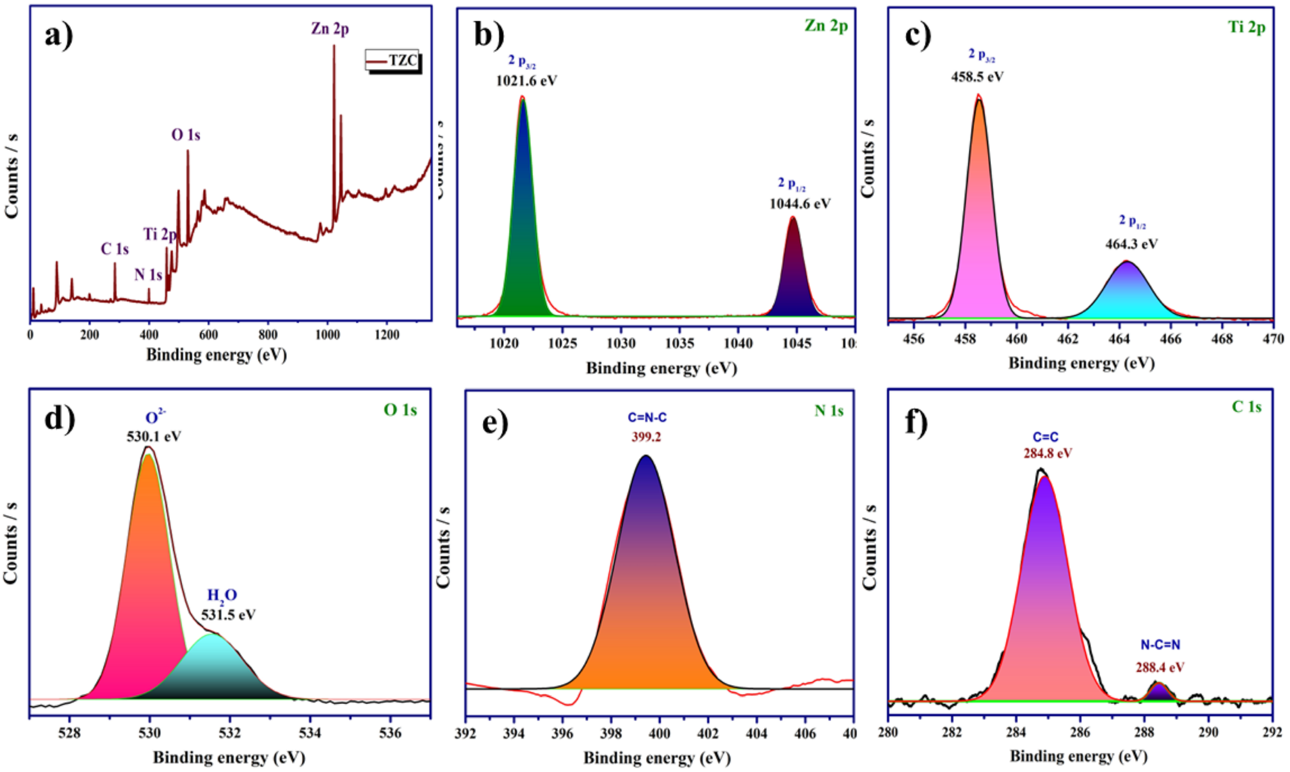

Fig. 4 XPS survey of TZC (a), high-resolution binding spectra of Zn 2p (b), Ti 2p (c), O 1s (d), N 1s (e), and C 1s (f).

3.1.5 XPS analysis. The X-ray photoelectron spectroscopy (XPS) analysis was performed to elucidate the surface chemical composition and oxidation states of the elements present in the TZC heterojunction presented in Fig. 4. The survey spectrum (Fig. 4a) confirms the presence of Zn, Ti, O, C, and N, indicating the successful incorporation of ZnO, TiO_2, and g-C_3N_4 within the composite. The high-resolution Zn 2p spectrum (Fig. 4b) exhibits two distinct peaks at 1021.6 (Zn $2p_{3/2}$) and 1044.6 eV (Zn $2p_{1/2}$), characteristic of Zn^{2+} in the wurtzite ZnO lattice.[41] The Ti 2p region (Fig. 4c) shows peaks at 458.5 and 464.3 eV corresponding to Ti $2p_{3/2}$ and Ti $2p_{1/2}$, respectively, confirming the presence of Ti^{4+} in anatase TiO_2.[42] The O 1s spectrum (Fig. 4d) revealed a main peak at 530.1 eV is attributed to lattice oxygen (O^{2-}), along with a higher binding-energy component at 531.5 eV assigned to surface hydroxyl groups and adsorbed water. These surface hydroxyls are known to play a crucial role in photocatalytic ROS generation. The N 1s spectrum (Fig. 4e) displays a prominent peak at 399.2 eV, corresponding to sp^2-hybridized C–N=C units in the heptazine structure of g-C_3N_4.[43] In the C 1s spectrum (Fig. 4f), the peak at 284.8 eV corresponds to adventitious carbon (C–C/C–H), while the additional peak at 288.4 eV arises from N–C=N bonds, further confirming the presence of g-C_3N_4. These chemical-state features collectively verify the successful fabrication of the ternary heterojunction and support its enhanced photocatalytic performance through improved charge-separation efficiency and reactive-species generation.

3.1.6 N_2 adsorption–desorption studies. The N_2 adsorption–desorption analysis of the TZC heterostructure in Fig. 5a exhibits a characteristic type IV isotherm accompanied by an H3-type hysteresis loop at higher relative pressures ($P/P_0 = 0.6$–0.8), indicative of a mesoporous network typically associated with slit-like pores formed by layered or plate-like structures. BET surface-area analysis shows that the composite possesses a relatively high specific surface area of 101.9 $m^2\ g^{-1}$, providing abundant accessible active sites for photocatalytic processes. The BJH pore-size distribution further confirms a dominant mesoporous structure, with an average pore diameter of 7.4 nm and a total pore volume of 0.19 cm^{-3}. Such a combination of high surface area, well-developed mesoporosity, and appreciable pore volume is advantageous for enhancing photocatalytic performance, as it promotes adsorption followed by diffusion, which facilitates the rearrangement of the pollutant molecules. It improves light-harvesting efficiency and supports rapid charge transport across TZC interfaces.

3.1.7 DR UV-vis and photoluminescence studies. The optical absorption properties of the TC and TZC composites were examined using diffuse-reflectance UV-vis spectroscopy, and presented in Fig. 5b. The spectra reveal a strong absorption in the UV region with a noticeable tail extending into the visible range for both materials. Compared with the binary TC sample, the ternary TZC heterostructure displays a slight red shift in the absorption edge and an overall enhancement in visible-light absorption, indicating improved light-harvesting capability upon incorporation of ZnO into the TiO_2/g-C_3N_4 matrix. The corresponding Tauc plots in Fig. 5c, constructed using the Kubelka–Munk transformed reflectance data and assuming direct allowed transitions, reveal optical band-gap energies of

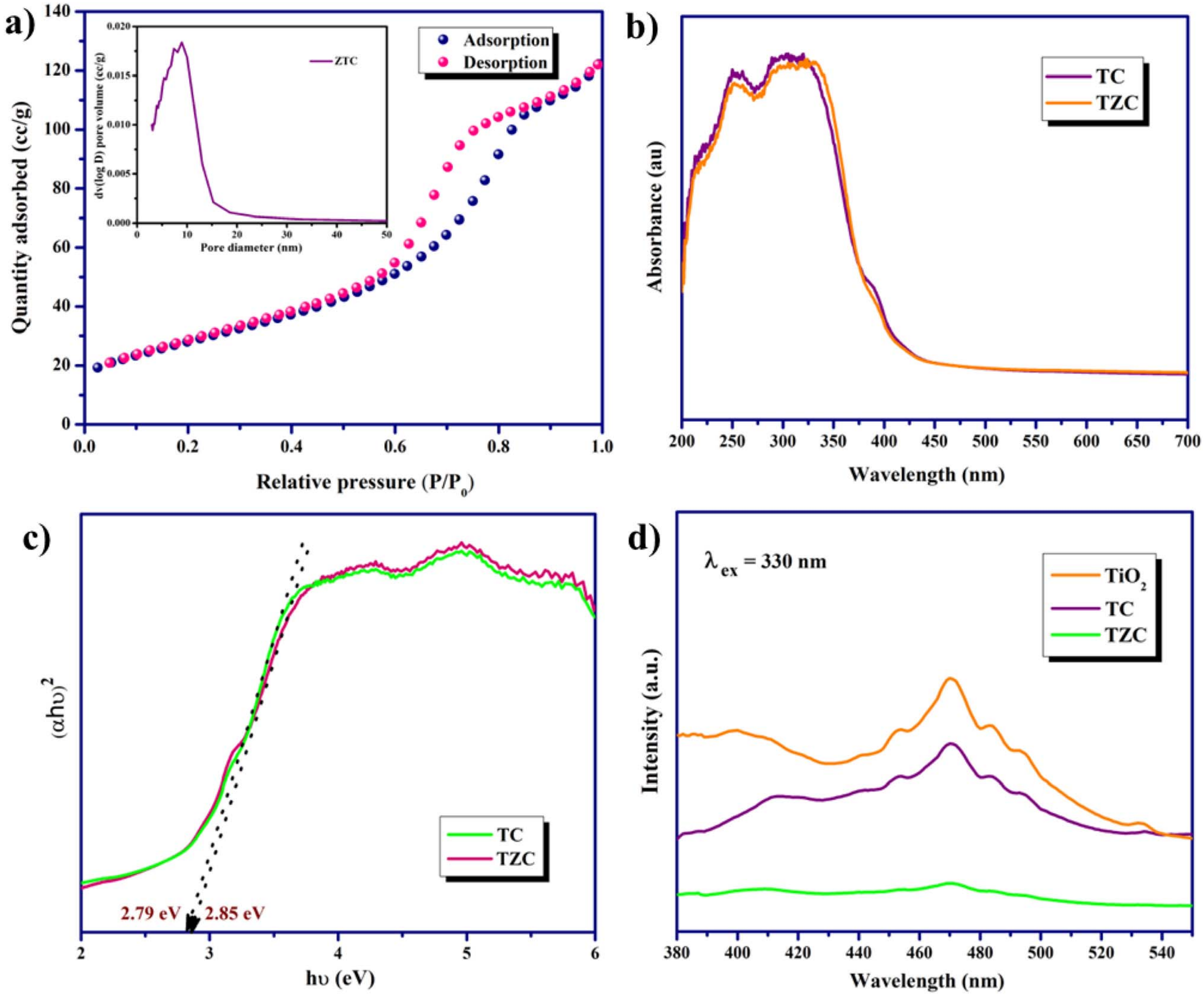

Fig. 5 N_2 adsorption–desorption isotherm (a), UV-vis DRS spectra (b), Tauc plot (c), and PL spectra (d) of catalysts.

2.85 eV for TC and 2.79 eV for TZC. The decrease of the band gap in TZC suggests enhanced electronic coupling and interfacial interaction in the ternary heterojunction. Such a reduction, combined with stronger visible-light absorption, is expected to facilitate higher photoexcited charge-carrier generation and promote more efficient charge separation within the dual S-scheme configuration.

The photoluminescence (PL) spectra of TiO_2, TC, and TZC are presented in Fig. 5d, which provides insight into the charge-carrier recombination behaviour within the photocatalysts. At an excitation wavelength of 330 nm, pure TiO_2 exhibits a strong PL emission peak centered around 460–480 nm, characteristic of rapid recombination of photogenerated electrons and holes. Upon coupling TiO_2 with g-C_3N_4 in the TC composite, the PL intensity decreases noticeably, indicating improved charge separation at the TiO_2/g-C_3N_4 interface. Especially, the ternary TZC heterostructure shows the lowest PL intensity among the samples, demonstrating a substantial suppression of radiative recombination. This pronounced quenching is attributed to the formation of a dual S-scheme heterojunction, which promotes spatially directed charge migration while retaining strong redox potentials. The enhanced interfacial interactions among ZnO, TiO_2, and g-C_3N_4 facilitate more efficient electron–hole separation and reduce recombination losses, thereby increasing the availability of reactive charge carriers for photocatalysis.

3.2 Structure and photocatalytic activity study of EtP

The photocatalytic degradation of ethyl paraben (EtP) was systematically evaluated by monitoring its UV-vis absorption spectra. The EtP solution exhibited a prominent absorption peak at 255 nm, corresponding to the $n \rightarrow \pi^*$ and π–π^* transitions of its aromatic moiety (Fig. 6a). Upon addition of the photocatalyst, a slight decrease in the absorbance was observed (~5%) even before irradiation, suggesting adsorption of EtP on the catalyst surface. During continuous light exposure, the characteristic EtP peak at 255 nm gradually decreased, reflecting the degradation of EtP molecules. This time-dependent reduction in spectral intensity signifies efficient photocatalytic

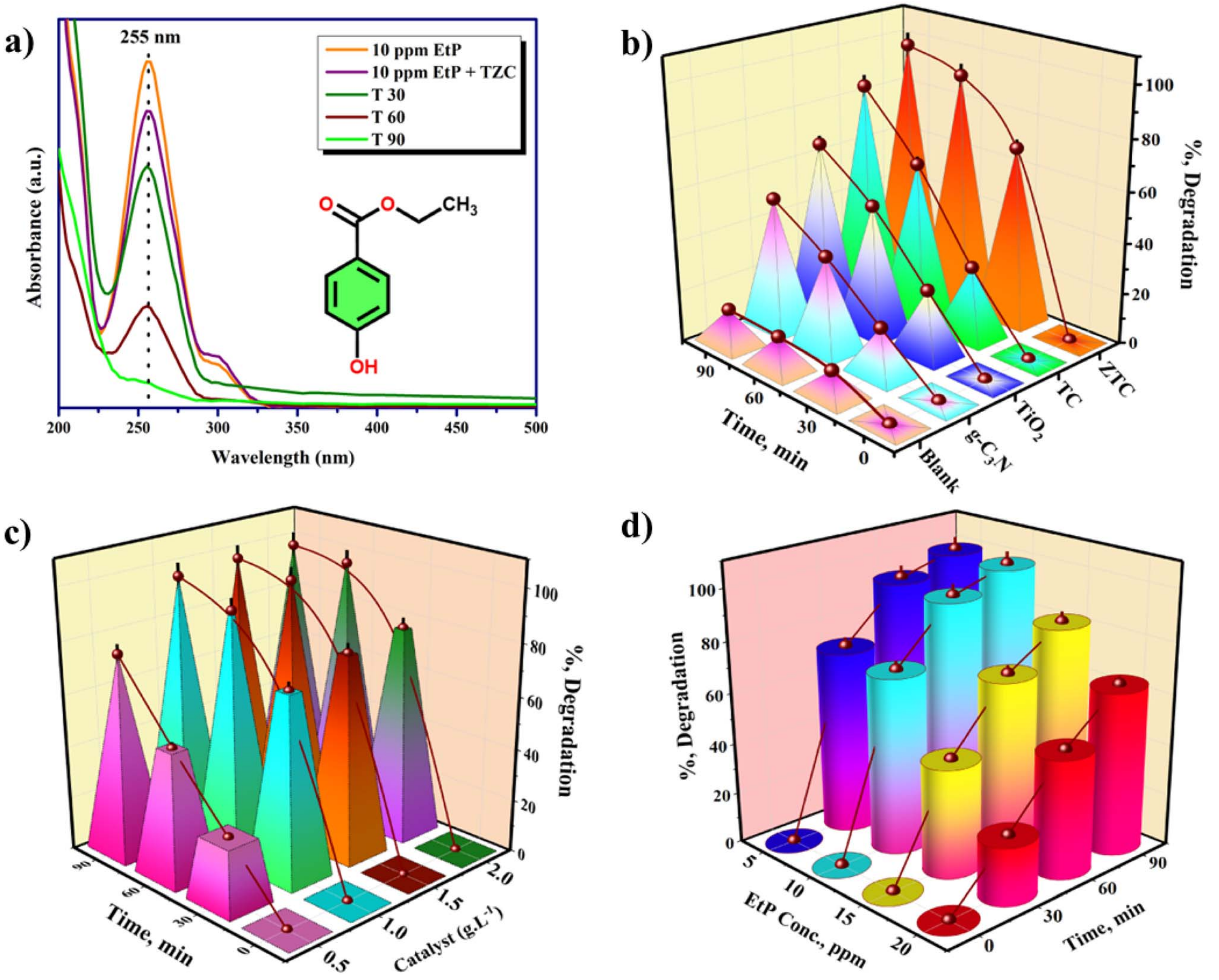

Fig. 6 Structure and UV-visible spectra of EtP (a), types of catalyst (b), TZC dosages (c), and initial EtP concentration (d) on the degradation efficiency of EtP, reaction parameters: EtP: 10 mg L^{-1}, catalyst: 1 g L^{-1}, duration: 0–90 min.

oxidation, ultimately leading to the complete breakdown and mineralization of EtP after 90 min of irradiation.

The comparative photocatalytic performance of the blank, g-C_3N_4, TiO_2, TC, and the ternary TZC heterostructure toward ethyl paraben (EtP) degradation over 90 min of irradiation is presented in Fig. 6b. As shown in the figure, the blank experiment exhibits minimal degradation of ~12%, confirming that photolysis alone does not contribute significantly to EtP removal. Pristine g-C_3N_4 and TiO_2 show moderate degradation efficiencies of 51% and 68%, respectively, reflecting their limited charge-separation capabilities and narrow visible-light response. The binary TC composite demonstrates enhanced degradation relative to the individual components, due to improved interfacial charge transfer at the heterojunction. Remarkably, the TZC ternary composite achieves the highest degradation efficiency, approaching nearly complete removal of EtP within 90 min. This superior performance is attributed to the formation of an effective dual S-scheme heterojunction among ZnO, TiO_2, and g-C_3N_4, which promotes efficient charge separation, suppresses recombination, and maximizes the generation of reactive oxygen species. The ascending degradation trend from single-component catalysts to the ternary system clearly demonstrates the synergistic effect of the integrated heterostructure in enhancing photocatalytic activity.

3.2.1 Influence of catalyst dosage. The effect of TZC catalyst dosage on the photocatalytic degradation of ethyl paraben (EtP) using the was systematically evaluated by varying the catalyst loading from 0.5 to 2.0 g L^{-1} at a fixed EtP concentration of 10 mg L^{-1}. As shown in Fig. 6c, the degradation efficiency increased significantly with catalyst dosage, primarily due to the availability of more active sites and more surface area. Although the complete degradation was observed at 1.5 g L^{-1} in a shorter time period, the dosage of 1.0 g L^{-1} also achieved complete mineralization within a span of 90 min. Beyond the optimal dosages, light-scattering effects, reduced photon penetration, and partial particle agglomeration begin to impede the accessibility and activation of the catalytic surface, leading to decreased catalytic efficiency. Therefore, while 1.5 g L^{-1}

represents the point of maximum degradation at a shorter time period, 1.0 g L^{-1} was selected as the optimized dosage because it provides a superior balance between photocatalytic activity and material efficiency. This dosage ensures optimal performance while avoiding excess catalyst consumption, aligning with the principles of atom economy and sustainability.

3.2.2 Effect of EtP concentration. The influence of initial EtP concentration on the photocatalytic performance of the TZC heterostructure is illustrated in Fig. 6d. At the lower concentration of 5 and 10 mg L^{-1}, the catalyst achieves complete degradation, owing to the availability of active sites and sufficient generation of reactive oxygen species. When the concentration is increased from the optimal dose of 10 mg L^{-1}, the degradation efficiency lowered to 82.57% and 64.03% for 15 and 20 mg L^{-1} of EtP, respectively. This decline is attributed to increased EtP molecules, saturation of active sites, and insufficient reactive species generation to sustain efficient degradation at elevated EtP levels. These observations confirm that the photocatalytic degradation of EtP by the TZC heterostructure is strongly dependent on the initial substrate concentration, with lower concentrations enabling more favourable catalyst and substrate interactions and enhanced degradation efficiency.

3.2.3 Effect of pH. The influence of initial solution pH on the photocatalytic degradation of ethylparaben (EtP) over the TZC heterojunction was evaluated in the pH range of 3–10 (Fig. S2, SI). The degradation efficiency increased from ~62% to ~76%, by changing pH from 3 to 5 and reached a maximum of ~98% at neutral pH 7. A subsequent decline in activity was observed in alkaline conditions, with degradation efficiencies, *i.e.*, ~81% at pH 8 and ~68% at pH 10. These results clearly demonstrate that the photocatalytic process is highly pH-dependent, with optimal performance under neutral conditions. The observed variation can be rationalized based on surface charge characteristics of the photocatalyst. At low pH, the catalyst surface becomes positively charged, contributing to the excessive protonation of surface hydroxyl groups, which may hinder the adsorption of EtP and suppress the formation of superoxide radicals ($^{\bullet}O_2^-$) due to competitive proton reduction. Additionally, higher H^+ concentration can promote recombination of photogenerated charge carriers, thereby reducing degradation efficiency. Under alkaline conditions, although the availability of OH^- ions may favor $^{\bullet}OH$ formation, excessive negative surface charge can lead to electrostatic repulsion effects and reduced adsorption affinity. Moreover, increased ionic strength and surface hydroxylation at high pH may accelerate charge recombination, ultimately lowering photocatalytic efficiency.

At neutral pH, a balanced surface charge condition enhances adsorption of EtP molecules and facilitates efficient separation of photogenerated electron–hole pairs within the dual S-scheme heterojunction. Furthermore, this pH range supports effective generation of photogenerated reactive species such as h^+ and $^{\bullet}O_2^-$, those are responsible for pollutant degradation. The superior activity at pH 7 is particularly advantageous from a practical standpoint, as most natural water systems exhibit near-neutral pH, indicating that the TZC photocatalyst can effectively operate under environmentally relevant conditions without the need for pH adjustment.

3.2.4 Heterogeneity and recyclability. The heterogeneous nature of the TZC photocatalyst was examined by conducting degradation experiments using the filtrate as well as the solid catalyst. The filtrate showed only ~5% degradation which is comparable to that observed under direct photolysis, indicating that the active catalytic process is predominantly heterogeneous, with negligible contribution from dissolved species. The reusability and stability of the catalyst were further assessed over six consecutive photocatalytic cycles, as presented in Fig. 7a. In the initial run, the catalyst achieved almost complete degradation of EtP. A minimal reduction in activity was observed in subsequent cycles, with efficiency decreasing by ~8% after the sixth run. This modest decline can be attributed to factors such as partial surface fouling, minor loss of catalyst during recovery, or a reduction in accessible active sites. The catalyst after the sixth run was characterized through different spectroscopic techniques such as XRD, FE SEM (Fig. S3 and S4, SI), and it showed its intact structural and morphological characteristics, underscoring its robustness and suitability for repeated use.

3.2.5 Kinetic study. The catalytic degradation of EtP was investigated by systematically altering the TZC loading and the initial concentration of EtP in order to understand the reaction kinetics. The experimental results exhibited an excellent fit to a first-order kinetic model, which can be expressed as:

$$\ln C_t = -kt + \ln C_0 \tag{2}$$

$$\ln\left(\frac{C_t}{C_0}\right) = -kt \tag{3}$$

Here, C_0 represents the initial concentration of EtP, C_t denotes the concentration at time t, k is the rate constant, and t is the reaction time measured in min.

As shown in Fig. 7b and c, plots of $\ln(C_t/C_0)$ *versus* time yielded straight lines for different EtP and TZC concentrations, clearly demonstrating first-order reaction behavior. The consistently high correlation coefficients ($R^2 \geq 0.98$) under all experimental conditions, as summarized in Table 1, further validate this kinetic model. The slopes of these linear plots correspond to the apparent rate constants, which exhibited a slight decline with increasing initial EtP concentration. This behavior may be attributed to reduced catalytic activity at higher pollutant levels, possibly due to competitive occupation of active sites on the TZC surface. Similarly, increasing the TZC dosage also enhanced the rate constant at a particular EtP concentration.

3.2.6 Scavengers study. The scavenging experiment provides valuable insight into the dominant reactive species involved in the photocatalytic degradation. To discern the role of each reactive oxygen species (ROS), various scavengers were introduced during the photocatalytic process, and the results are presented in Fig. 7d. Potassium iodide (KI) and isopropyl alcohol (IPA) were used to quench hydroxyl radicals ($^{\bullet}OH$) whereas sodium oxalate and *p*-benzoquinone (*p*-BQN) were used as scavengers for photogenerated holes (h^+) and

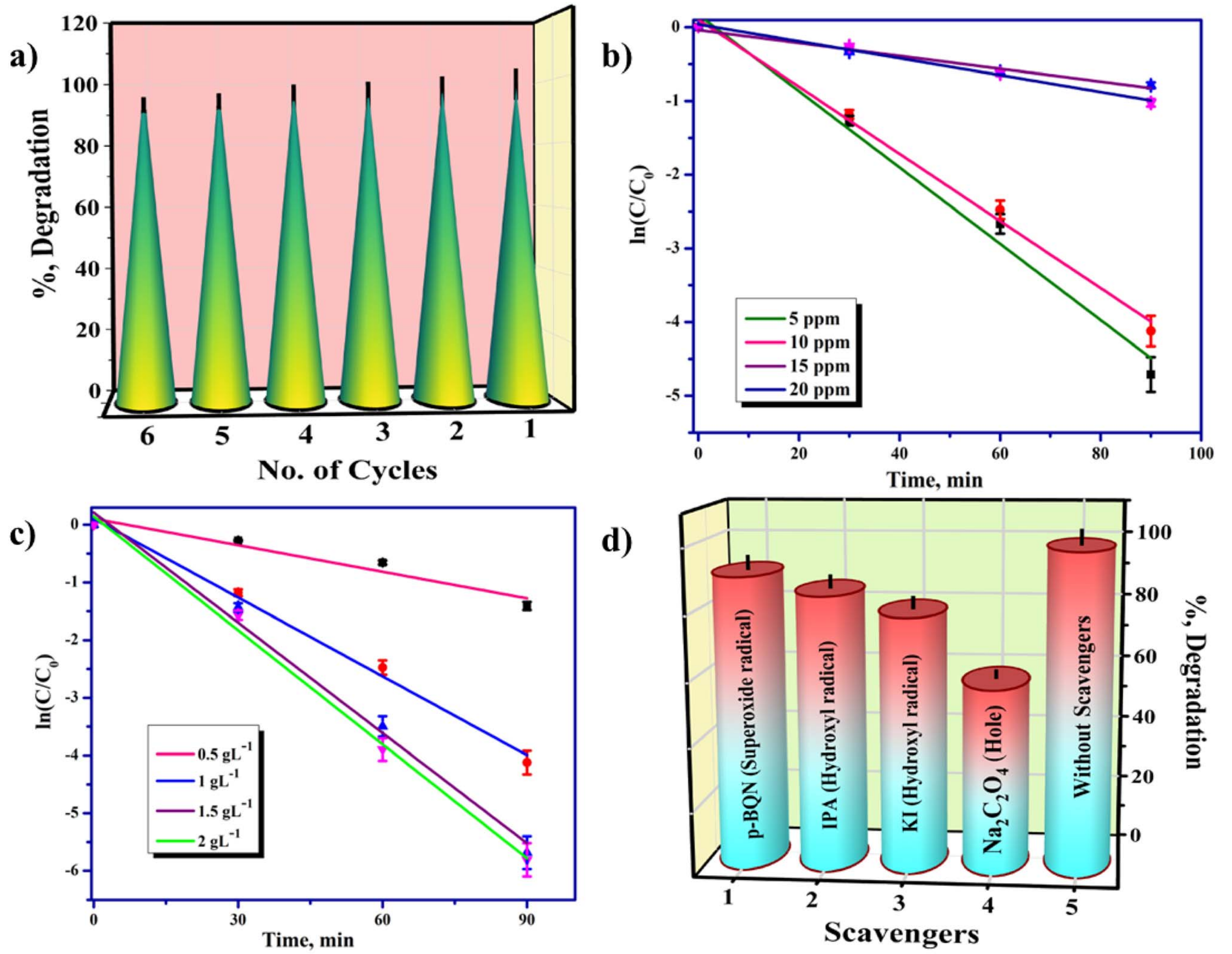

Fig. 7 Recycling of TZC catalyst (a), kinetic study (b and c), and effect of scavengers (d) for the degradation of EtP, Reaction parameters: EtP: 10 mg L^{-1}, catalyst: 1 g L^{-1}, duration: 0–90 min.

Table 1 Relationship between the rate constant with TZC and EtP dosages

Sl. No.	EtP (mg L^{-1})	TZC (g L^{-1})	Rate constant (k, s^{-1})	R^2
1	5	1	0.0518	0.986
2	10	1	0.0455	0.993
3	15	1	0.0217	0.983
4	20	1	0.0115	0.991
5	10	0.5	0.0154	0.945
6	10	1.5	0.0637	0.989
7	10	2	0.0659	0.995

superoxide radicals ($^{\bullet}O_2^-$), respectively. As observed in the degradation profile, the presence of sodium oxalate resulted in the most pronounced decrease in degradation efficiency, reducing it to 57%. This significant suppression confirms that holes are the primary oxidative species driving EtP degradation. The degradation efficiency in the presence of KI and IPA decreased to approximately 78% and 84%, respectively, indicating a considerable yet secondary contribution of hydroxyl radicals in the reaction mechanism. Moreover, the addition of p-BQN caused a minimal fall in activity around 90%, suggesting that superoxide radicals play a negligible role in the degradation pathway. Overall, these findings reveal that the photocatalytic degradation of EtP is predominantly governed by hole-driven oxidation processes, followed by hydroxyl radical-induced reactions, while the involvement of superoxide radicals appears to be minimal under the studied conditions.

3.2.7 Intermediates and plausible degradation pathway of EtP. The intermediates formed during the photocatalytic degradation of EtP were identified using liquid chromatography mass spectrometry (LC MS), and the obtained mass spectrum was presented in Fig. S5 (SI). EtP contains several electron-rich functional moieties, such as a phenolic hydroxyl group, an aromatic ring, a conjugated alkene system, and ester functionalities, those are highly susceptible to oxidative attack by reactive oxygen species (ROS) generated under photocatalytic conditions, such as photogenerated holes (h^+), hydroxyl radicals ($^{\bullet}OH$), and superoxide radicals ($^{\bullet}O_2^-$). Based on the detected intermediates and their *m*/*z* values, and supported by available

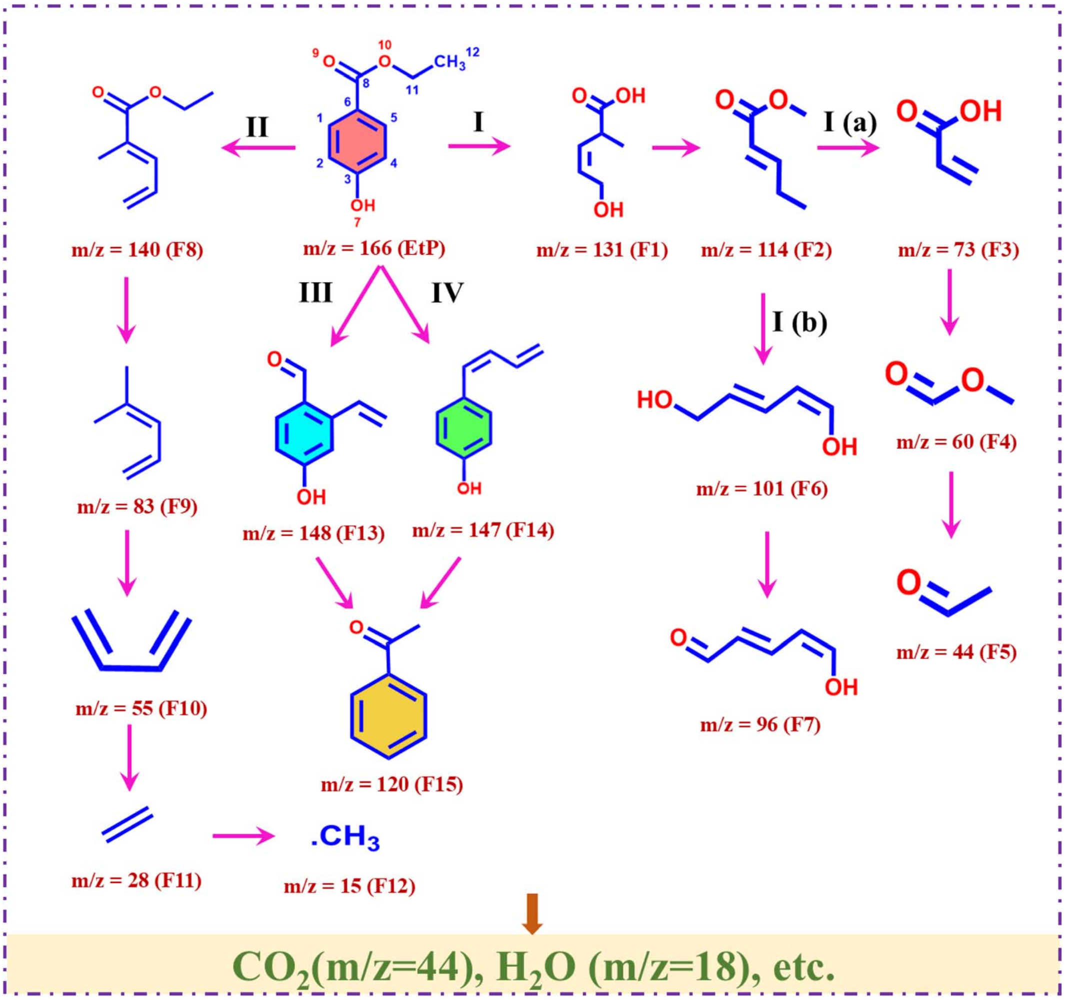

Scheme 2 Plausible fragmentation pathway of EtP degradation.

literature, four plausible degradation pathways (Paths I–IV) were proposed, as illustrated in Scheme 2.

Path I depicted the ROS-induced cleavage of the ester side chain of EtP ($m/z = 166$), forming intermediate F1 ($m/z = 131$). Subsequent oxidation, decarboxylation, and C–C bond scission yield progressively smaller oxygenated fragments, including F2 ($m/z = 114$) and F3 ($m/z = 73$). These intermediates further undergo oxidative fragmentation through path I(a) to produce low-molecular-weight species such as F4 ($m/z = 60$) and F5 ($m/z = 44$). In a parallel sub-route [Path I(b)], hydroxylation and oxidative cleavage of F2 generate dihydroxy unsaturated intermediates (F6, $m/z = 101$), which are further oxidized to F7 ($m/z = 96$) before undergoing mineralization. Path II involves ester hydrolysis followed by oxidative cleavage of the conjugated alkene system, leading to the formation of intermediate F8 ($m/z = 140$). Continued C–C bond cleavage produces unsaturated hydrocarbon fragments such as F9 ($m/z = 83$) and F10 ($m/z = 55$), which are ultimately oxidized to small alkyl species, including F11 ($m/z = 28$) and F12 ($m/z = 15$). Path III proceeds *via* hydrolysis of the ester of EtP followed by rearrangement resulting in F13 ($m/z = 148$). Dealkylation of this intermediate leads to oxygenated aromatic fragments that subsequently undergo side-chain cleavage. Path IV involves oxidative dealkylation and side-chain cleavage of EtP to form substituted aromatic intermediates such as F14 ($m/z = 147$). Intermediates generated in Paths III and IV converge to yield a common aromatic ketone, F15 ($m/z = 120$). In the final stages, all aromatic and aliphatic intermediates undergo successive oxidation, decarboxylation, and bond cleavage, resulting in complete mineralization to CO_2 ($m/z = 44$), H_2O ($m/z = 18$), and other low-molecular-weight products.

3.2.8 Proposed dual S-scheme charge transfer mechanism.

Based on the band structure analysis and photocatalytic performance, a dual S-scheme heterojunction charge transfer mechanism is proposed for the TiO_2/ZnO/g-C_3N_4 (TZC) photocatalyst, as illustrated in Scheme 3. Before interfacial contact, TiO_2, g-C_3N_4, and ZnO possess distinct Fermi energy levels and band edge positions.[44] Upon contact, electrons migrate from g-C_3N_4 to TiO_2 and ZnO until Fermi level equilibration is achieved, resulting in the formation of built-in internal electric fields (IEF) and band bending at both interfaces.[45,46] Under sunlight exposure, all three semiconductors are photoexcited, generating electron–hole pairs. Due to the combined effects of the IEF and interfacial coulombic attraction, photogenerated

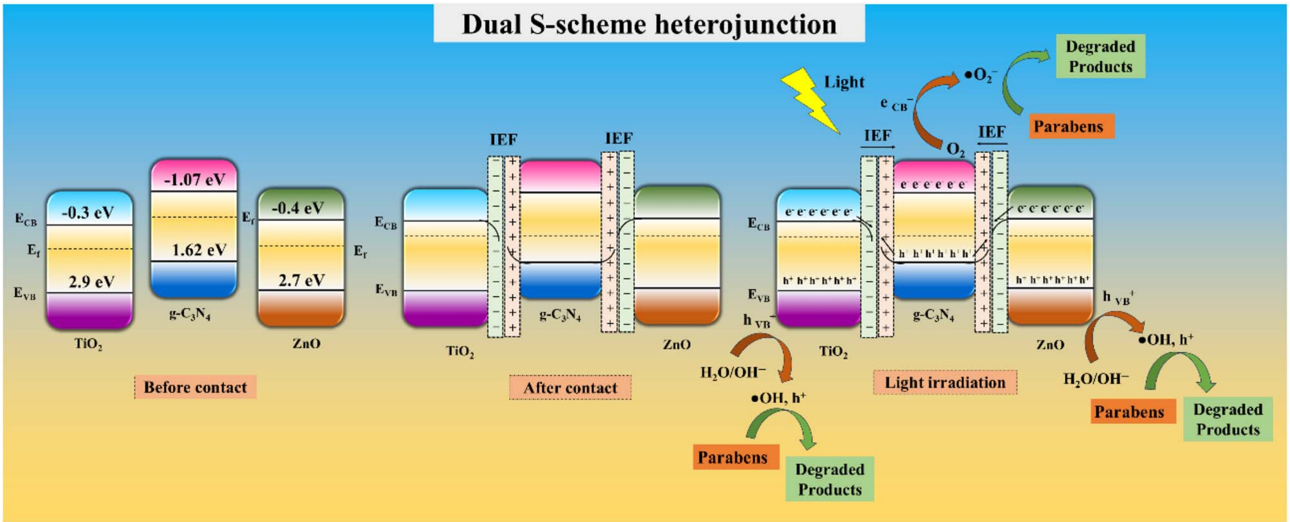

Scheme 3 Proposed dual S-scheme charge transfer mechanism for EtP degradation.

electrons in the conduction bands of TiO_2 and ZnO preferentially recombine with photogenerated holes in the valence band of $g-C_3N_4$.[47] This selective interfacial recombination through dual S-scheme mechanism suppresses bulk charge recombination while preserving the highly reductive electrons in the conduction band of $g-C_3N_4$ and the highly oxidative holes in the valence bands of TiO_2 as well as ZnO. Consequently, the accumulated electrons in $g-C_3N_4$ reduce dissolved O_2 to generate $^•O_2^-$ radicals, while the retained holes in TiO_2 and ZnO oxidize surface-adsorbed H_2O or OH^- to produce $^•OH$ radicals. These highly reactive oxygen species cooperatively drive the oxidative degradation and mineralization of parabens into low-molecular-weight products. To experimentally validate the proposed band alignment, Mott–Schottky measurements were performed for TiO_2, ZnO, and $g-C_3N_4$. The positive slopes of the M–S plots confirm the n-type nature of all three semiconductors, and the flat-band potentials were also estimated (Fig. S6, SI). These calculated band-edge potentials are consistent with the proposed dual S-scheme configuration, thereby providing experimental support for the interfacial charge transfer pathway illustrated in the mechanism diagram. Overall, the dual S-scheme heterojunction effectively promotes charge separation, maintains high redox capability, and accounts for the enhanced photocatalytic activity observed in the ternary system.

4. Conclusion

This study demonstrates the effective degradation of the synthetic preservative ethyl paraben (EtP), a prevalent endocrine-disrupting contaminant in aquatic environments, using a rationally designed dual S-scheme TZC composite photocatalyst under sunlight irradiation. The developed catalyst was comprehensively characterized to elucidate its structural and morphological features. Complete degradation of EtP was achieved under optimized conditions, and key operational parameters influencing the photocatalytic process were systematically evaluated. The TZC heterostructure exhibited significantly enhanced photocatalytic activity compared with its individual components, underscoring the critical role of interfacial electronic interactions and the synergistic effects arising from dual S-scheme heterojunction formation. Reactive species trapping experiments confirmed that photogenerated holes (h^+) and hydroxyl radicals ($^•OH$) are the dominant active species responsible for EtP degradation. Furthermore, the TZC composite demonstrated excellent durability and reusability, with negligible activity loss observed over multiple photocatalytic cycles.

Overall, this work highlights the effectiveness of dual S-scheme heterojunction engineering in overcoming the intrinsic limitations of conventional photocatalysts. The high photocatalytic efficiency, structural stability, and solar-light responsiveness of the TZC photocatalyst indicate its strong potential for sustainable water purification and the mitigation of paraben-based emerging contaminants, offering a promising strategy for advanced environmental remediation applications.

Author contributions

Mano Ranjan Barik: material preparation, investigation, methodology, software, writing–original draft, data curation. Anshuman Sarangi: material preparation, investigation. Sushanta Kumar Badamali: supervision, conceptualization, methodology, writing–review & editing, formal analysis.

Conflicts of interest

There are no conflicts to declare.

Data availability

The supporting data has been provided as part of the supplementary information (SI). Supplementary information: EDAX pattern of TZC heterojunction (Fig. S1), effect of pH variation on the degradation efficiency of EtP (Fig. S2), XRD analysis of TZC synthesized and regenerated (Fig. S3), FE SEM analysis of regenerated TZC (Fig. S4), LCMS spectra of EtP degradation (Fig. S5), Mott–Schottky analysis of ZnO, TiO_2, g-C_3N_4 individually (Fig. S6), comparative table for the photocatalytic degradation of EtP (Table S1). See DOI: https://doi.org/10.1039/d6ra00767h.

Acknowledgements

MB deeply acknowledges the Center of Advanced Materials and Applications, Department of Chemistry, Utkal University, for providing research facilities. MB is thankful to the Central Research Facility, KIIT University, for the XRD and LC-MS analysis. MB thanks to NIT Rourkela for FE SEM and BET analysis, and also IIT Hyderabad for assistance with XPS analysis. MB also acknowledges the use of ChatGPT, an AI tool by OpenAI, for its support in language polishing and sentence refinement for enhancing the readability of this manuscript. MB gratefully acknowledges the University Grant Commission, Government of India, for the award of a Senior Research Fellowship to pursue doctoral work.

References

1 X. Zhou, X. Zhou, C. Wang and H. Zhou, *Chemosphere*, 2023, **313**, 137489.
2 A. Jha and M. Jha, *Int. J. Nurs. Inf.*, 2024, **3**, 9–21.
3 A. Barbulova, G. Colucci and F. Apone, *Cosmetics*, 2015, **2**, 82–92.
4 N. A. Vita, C. A. Brohem, A. D. P. M. Canavez, C. F. S. Oliveira, O. Kruger, M. Lorencini and C. M. Carvalho, *Toxicol. Lett.*, 2018, **287**, 70–82.
5 C. Juliano and G. A. Magrini, *Cosmetics*, 2017, **4**, 11.
6 L. K. Al-Halaseh, S. Al-Adaileh, A. Mbaideen, M. N. A. Hajleh, A. Al-Samydai, Z. Z. Zakaraya and W. A. Dayyih, *J. Cosmet., Dermatol.*, 2022, **21**, 3265–3271.
7 A. Pal, P. Panda and S. Mukkamala, *Int. J. Manag.*, 2020, **11**, 1–10.
8 N. Matwiejczuk, A. Galicka and M. M. Brzóska, *J. Appl. Toxicol.*, 2020, **40**, 176–210.
9 A. F. Fransway, P. J. Fransway, D. V. Belsito and J. A. Yiannias, *Dermatitis*, 2019, **30**, 32–45.
10 R. Golden, J. Gandy and G. Vollmer, *Crit. Rev. Toxicol.*, 2005, **35**, 435–458.
11 T. M. K. Ahmed and M. M. Bakr, *Sci. Res. J. Pharm.*, 2022, **2**(5), 1–14.
12 S. A. Q. Alkafajy and R. A. A. Abdul-Jabbar, *Ann. Trop. Med. Public Health*, 2020, **23**, SP232242.
13 H. Yamamoto, I. Tamura, Y. Hirata, J. Kato, K. Kagota, S. Katsuki, *et al.*, *Sci. Total Environ.*, 2011, **410**, 102–111.
14 C. Haman, X. Dauchy, C. Rosin and J. F. Munoz, *Water Res.*, 2015, **68**, 1–11.
15 E. M. Ngigi, P. N. Nomngongo and J. C. Ngila, *Int. J. Environ. Sci. Technol.*, 2022, **19**, 2139–2154.
16 K. Vellingiri, V. Choudhary, D. W. Boukhvalov and L. Philip, *ACS ES&T Water*, 2022, **2**, 1475–1499.
17 S. A. Khan, M. Jain, K. K. Pant, Z. M. Ziora and M. A. Blaskovich, *Sci. Total Environ.*, 2024, **920**, 171020.
18 Z. Yang, X. Liu, X. Hao, H. Yin, Y. Li and G. Zhang, *Appl. Catal., B*, 2026, **386**, 126389.
19 M. R. Barik and S. K. Badamali, *ChemistrySelect*, 2025, **10**, e01792.
20 M. T. Yifira, G. Gebreslassie, A. K. Mersha and K. N. Mekonnen, *RSC Adv.*, 2025, **15**, 22649–22660.
21 G. Wu, W. Zhang, Z. Mo, X. Zhao, P. Sun, Q. Wang, *et al.*, *ACS Catal.*, 2025, **15**, 8822–8832.
22 Q. Wang, G. Wu, P. Zheng, L. Pan, Z. Mo, P. Sun, *et al.*, *Nano Mater. Sci.*, 2025, **8**, 234–243.
23 J. Huang, P. Yan, X. Zhu, G. Wu, J. Dong, E. Zhang, *et al.*, *J. Mater. Sci. Technol.*, 2026, **269**, 306–317.
24 R. Ahmad, Z. Ahmad, A. U. Khan, N. R. Mastoi, M. Aslam and J. Kim, *J. Environ. Chem. Eng.*, 2016, **4**, 4143–4164.
25 S. He, Y. Du, C. Li, C. Li, J. Li, J. Sunarso, *et al.*, *RSC Adv.*, 2025, **15**, 21142–21155.
26 H. Wang, L. Zhang, Z. Chen, J. Hu, S. Li, Z. Wang, *et al.*, *Chem. Soc. Rev.*, 2014, **43**, 5234–5244.
27 Q. Xu, L. Zhang, B. Cheng, J. Fan and J. Yu, *Chem*, 2020, **6**, 1543–1559.
28 R. Daghrir, P. Drogui and D. Robert, *Ind. Eng. Chem. Res.*, 2013, **52**, 3581–3599.
29 I. Ahmad, R. Bousbih, A. Mahal, W. Q. Khan, M. Aljohani, M. A. Amin, *et al.*, *Mater. Sci. Semicond. Process.*, 2024, **180**, 108578.
30 Y. Li, M. Zhou, B. Cheng and Y. Shao, *J. Mater. Sci. Technol.*, 2020, **56**, 1–17.
31 L. Zhang, J. Zhang, H. Yu and J. Yu, *Adv. Mater.*, 2022, **34**, 2107668.
32 Q. Xu, L. Zhang, B. Cheng, J. Fan and J. Yu, *Chem*, 2020, **6**, 1543–1559.
33 A. Petala, R. Bontemps, A. Spartatouille, Z. Frontistis, M. Antonopoulou, I. Konstantinou, *et al.*, *Catal. Today*, 2017, **280**, 122–131.
34 Z. Frontistis, M. Antonopoulou, A. Petala, D. Venieri, I. Konstantinou, D. I. Kondarides and D. Mantzavinos, *J. Hazard. Mater.*, 2017, **323**, 478–488.
35 X. Liu and X. Wang, *J. Mol. Liq.*, 2024, **409**, 125530.
36 M. R. Barik, J. Kumar and S. K. Badamali, *RSC Sustain.*, 2025, **3**, 3582–3600.
37 B. S. Shirke, P. V. Korake, P. P. Hankare, S. R. Bamane and K. M. Garadkar, *J. Mater. Sci.: Mater. Electron.*, 2011, **22**, 821–824.
38 S. Lenka and S. K. Badamali, *Mol. Catal.*, 2023, **536**, 112918.
39 A. Gnanaprakasam, V. M. Sivakumar, P. L. Sivayogavalli and M. Thirumarimurugan, *Ecotoxicol. Environ. Saf.*, 2015, **121**, 121–125.
40 F. Chang, Y. Xie, C. Li, J. Chen, J. Luo, X. Hu and J. Shen, *Appl. Surf. Sci.*, 2013, **280**, 967–974.
41 R. Al-Gaashani, S. Radiman, A. R. Daud, N. Tabet and Y. Al-Douri, *Ceram. Int.*, 2013, **39**, 2283–2292.
42 L. Ren, Y. Li, M. Mao, L. Lan, X. Lao and X. Zhao, *Appl. Surf. Sci.*, 2019, **490**, 283–292.
43 S. Fang, Y. Xia, K. Lv, Q. Li, J. Sun and M. Li, *Appl. Catal., B*, 2016, **185**, 225–232.

44 Y. Yuan, R. T. Guo, L. F. Hong, Z. D. Lin, X. Y. Ji and W. G. Pan, *Chemosphere*, 2022, **287**, 132241.

45 Q. Xu, L. Zhang, B. Cheng, J. Fan and J. Yu, *Chem*, 2020, **6**, 1543–1559.

46 H. Ren, A. Labidi, T. Chang, Z. Miao, X. Feng and C. Wang, *Coord. Chem. Rev.*, 2026, **548**, 217183.

47 J. Wang, Q. Hao, R. Yang, X. Niu, R. Wang, L. Yang and Y. Wu, *Appl. Catal., B*, 2024, **356**, 124232.